Dynamic subunit turnover in ESCRT-III assemblies is regulated by Vps4 to mediate membrane remodelling during cytokinesis

Beata Mierzwa, Nicolas Chiaruttini, Lorena Redondo-Morata, Joachim Moser von Filseck, Julia König, Jorge Larios, Ina Poser, Thomas Müller-Reichert, Simon Scheuring, Aurelien Roux, et al.

To cite this version:

Beata Mierzwa, Nicolas Chiaruttini, Lorena Redondo-Morata, Joachim Moser von Filseck, Julia König, et al.. Dynamic subunit turnover in ESCRT-III assemblies is regulated by Vps4 to mediate membrane remodelling during cytokinesis. Nature Cell Biology, 2017, 19 (7), pp.787 - 798. 10.1038/ncb3559 . inserm-01653774

HAL Id: inserm-01653774
https://inserm.hal.science/inserm-01653774

Submitted on 1 Dec 2017

HAL is a multi-disciplinary open access archive for the deposit and dissemination of scientific research documents, whether they are published or not. The documents may come from teaching and research institutions in France or abroad, or from public or private research centers.

L'archive ouverte pluridisciplinaire **HAL**, est destinée au dépôt et à la diffusion de documents scientifiques de niveau recherche, publiés ou non, émanant des établissements d'enseignement et de recherche français ou étrangers, des laboratoires publics ou privés.

Dynamic subunit turnover in ESCRT-III assemblies is regulated by Vps4 to mediate membrane remodelling during cytokinesis

Authors:

Beata E. Mierzwa[1*], Nicolas Chiaruttini[2*], Lorena Redondo-Morata[3*], Joachim Moser von Filseck[2], Julia König[4,5], Jorge Larios[2], Ina Poser[6], Thomas Müller-Reichert[4], Simon Scheuring[3,7], Aurélien Roux[2,8,9], Daniel W. Gerlich[1,9]

Affiliations:

[1]Institute of Molecular Biotechnology of the Austrian Academy of Sciences (IMBA), Vienna Biocenter (VBC), AT-1030 Vienna, Austria. [2]Department of Biochemistry, University of Geneva, CH-1211 Geneva, Switzerland. [3]U1006 INSERM, Aix-Marseille Université, 13009 Marseille, France. [4]Experimental Center, Medical Faculty Carl Gustav Carus, Technische Universität Dresden, D-01307 Dresden, Germany. [5]Present address: Electron Microscopy Unit, Francis Crick Institute, London, United Kingdom. [6]Max Planck Institute of Molecular Cell Biology and Genetics, D-01307 Dresden, Germany. [7]Present address: departments of Anesthesiology and Physiology & Biophysics, Weill Cornell Medicine, New York, NY 10065, USA. [8]Swiss National Centre for Competence in Research Programme Chemical Biology, CH-1211 Geneva, Switzerland.

[*]These authors contributed equally to this work

[9]Correspondence should be addressed to aurelien.roux@unige.ch and daniel.gerlich@imba.oeaw.ac.at

ABSTRACT

The Endosomal Sorting Complex Required for Transport (ESCRT)-III mediates membrane fission in fundamental cellular processes, including cytokinesis. ESCRT-III is thought to form persistent filaments that over time increase their curvature to constrict membranes. Unexpectedly, we found that ESCRT-III at the midbody of human cells rapidly turns over subunits with cytoplasmic pools while gradually forming larger assemblies. ESCRT-III turnover depended on the ATPase VPS4, which accumulated at the midbody simultaneously with ESCRT-III subunits, and was required for assembly of functional ESCRT-III structures. *In vitro*, the Vps2/Vps24 subunits of ESCRT-III formed side-by-side filaments with Snf7 and inhibited further polymerization, but the growth inhibition was alleviated by the addition of Vps4 and ATP. High-speed atomic force microscopy further revealed highly dynamic arrays of growing and shrinking ESCRT-III spirals in presence of Vps4. Continuous ESCRT-III remodeling by subunit turnover might facilitate shape adaptions to variable membrane geometries, with broad implications for diverse cellular processes.

INTRODUCTION

The Endosomal Sorting Complex Required for Transport-III (ESCRT-III) promotes membrane fission from the inner side of membrane necks in various cellular processes[1], including the biogenesis of multivesicular bodies[2], cytokinetic abscission[3-7], nuclear envelope sealing[8-11], plasma membrane repair[12], HIV budding[13,14], and exosome or microvesicle shedding[15-17]. ESCRT-III forms polymers that are thought to constrict membrane necks until they split[18-25], but the mechanism underlying constriction is unknown.

ESCRT-III is evolutionary conserved from humans to archaea, and is composed of four structurally related core subunits with distinct functions[18-27]. Budding yeast Vps20 (human homolog is CHMP6) functions as a nucleation factor, Snf7 (human homolog CHMP4 has three isoforms, A-C) serves as a main polymer subunit, Vps24 (CHMP3 in humans) and Vps2 (CHMP2A and B isoforms in humans) inhibit Snf7 polymerization[28-32] and recruit the ATPase Vps4, which is thought to predominantly disassemble ESCRT-III polymers[30,31,33-38]. How different ESCRT-III components coordinately assemble and remodel polymer structures has remained unclear.

Purified ESCRT-III subunits polymerize into filaments that form spirals on flat membranes or helices on membrane tubes[36,39-45]. ESCRT-III also forms filament spirals and helices in intact cells[44,46,47], and it is required for the assembly of large filament helices that constrict the intercellular bridge during cytokinetic abscission[4].

Prevailing models propose that ESCRT-III mediates membrane fission by sequential assembly of distinct subunits[18-23,25], whereby late-binding Vps2/Vps24 (CHMP2/CHMP3) subunits might form a rigid dome-shaped scaffold to guide attached membranes towards the fission site[36] or induce changes in the curvature of pre-assembled Snf7 filament spirals to promote membrane neck constriction[41]. These models rely on the sequential addition of distinct subunits and the persistence of ESCRT-III polymers, yet this has not been directly observed under physiological conditions. We hence set out to systematically quantify the assembly kinetics, dynamics, and structure of ESCRT polymers in live human cells and in an *in vitro* reconstitution system.

RESULTS

ESCRT-III assemblies continuously turn over their subunits with the cytoplasm

To investigate the dynamics of ESCRT-III polymers at the abscission site, we generated stable HeLa cell lines expressing fluorescently tagged subunits. We found that CHMP4B tagged with GFP via a long flexible linker (Localization and Affinity Purification tag, LAP) and expressed close to endogenous levels[4] did not perturb abscission (Fig. 1a). To probe the functionality of LAP-tagged CHMP4B, we depleted endogenous CHMP4B in wild-type HeLa cells or in HeLa cells stably expressing siRNA-resistant mouse CHMP4B-LAP (Supplementary Fig. 1a). Cytokinetic abscission was substantially perturbed upon depletion of endogenous CHMP4B in wild-type HeLa cells, but was not affected in mouse-CHMP4B-LAP-expressing HeLa cells (Fig. 1a), validating the functionality of CHMP4B-LAP.

We next investigated the dynamics of midbody-localized ESCRT-III by fluorescence recovery after photobleaching (FRAP) experiments. Unexpectedly, we found that CHMP4B-LAP rapidly re-accumulated at the midbody following photobleaching (Fig. 1b, c and Supplementary Video 1). A single exponential function constrained to initial fluorescence values did not fit the FRAP kinetics (Fig. 1c), indicating the presence of two populations of CHMP4B-LAP with distinct residence times at the midbody. We determined the residence times for the two midbody-localized fractions by a double-exponential fit (Fig. 1b, h, i). A highly mobile fraction of 64 ± 6% (mean ± SEM, as in the rest of the paper, if not otherwise noted) of CHMP4B-LAP had a residence time of 19.5 ± 2.7 s, whereas a stably-bound fraction of 36 ± 2% had a residence time of 716.0 ± 91.3 s. Modeling the stably-bound fraction as completely immobile also yielded a good approximation (Supplementary Fig. 1b, c). Importantly, both methods of model fitting yielded consistent values for the fraction and residence time of the highly mobile pool

(Supplementary Fig. 1d). Thus, the majority of CHMP4B-LAP molecules at the midbody continuously turns over with a cytoplasmic pool – at a rate up to two orders of magnitude faster than the macroscopic accumulation of ESCRT-III at the midbody[4,5].

ESCRT-III initially localizes within two cortical regions adjacent to the midbody, which later constrict to split the plasma membrane[4,5]. Photobleaching of CHMP4B-LAP prior to or during constriction stages revealed similar recovery kinetics (Fig. 1b, d, e, and Supplementary Video 1), indicating that midbody-localized ESCRT-III dynamically turns over subunits with cytoplasmic pools during its macroscopic accumulation and constriction.

We next investigated the localization and dynamics of other ESCRT-III subunits. We tagged human CHMP2B, CHMP3 and CHMP4B with the same design used for tagging mouse CHMP4B. All three LAP-tagged ESCRT-III subunits localized to the midbody (Fig. 2f, g, and Supplementary Video 2) and did not perturb abscission (Supplementary Fig. 2a-d). CHMP2B, CHMP3, and CHMP4B subunits accumulated at the midbody with indistinguishable kinetics (Fig. 2f, g, and Supplementary Video 2). Hence, ESCRT-III assembles at the midbody with a fairly constant proportion of different core subunits during the progression of abscission.

We next probed the dynamics of human CHMP2B, CHMP3, and CHMP4B at the midbody. FRAP experiments showed that all three subunits had highly mobile fractions with residence times similar to mouse CHMP4B (Fig. 1h, i, and Supplementary Fig. 2g-i). We noticed somewhat variable kinetics at late stages of FRAP recovery, which resulted in inaccurate fitting of single exponential functions (Supplementary Fig. 2e-g). Given the technical difficulty to accurately measure long residence times, the relevance of the observed variations remains unclear. Importantly, however, all FRAP experiments consistently show that highly mobile fractions of CHMP2B, CHMP3, and CHMP4B dynamically turn over with similar residence times. Overall, our experiments show that ESCRT-III forms highly dynamic assemblies at the midbody.

Dynamic subunit turnover in ESCRT-III assemblies depends on VPS4

We wondered if VPS4 could be responsible for ESCRT-III turnover, as it is the only known nucleotide hydrolase in the ESCRT-III pathway[30,33]. VPS4 was previously detected at the midbody only during late stages of abscission[5], which would be inconsistent with its contribution to the high ESCRT-III turnover observed during early stages. However, previous measurements of VPS4 accumulation were based on overexpression from a viral promoter[5], which could limit its detection at the midbody owing to high cytoplasmic background. We thus re-examined VPS4 accumulation in cells stably expressing LAP-tagged murine VPS4B from its endogenous promoter (Supplementary Fig. 3a). In these cells, VPS4B-LAP indeed accumulated at the midbody simultaneously with CHMP4B-LAP (Fig. 2a, b, and Supplementary Video 3). Thus, VPS4 is present at early stages and could contribute to ESCRT-III dynamics throughout the entire abscission process.

To investigate the role of VPS4 in ESCRT-III dynamics, we depleted both isoforms VPS4A and VPS4B in CHMP4B-LAP-expressing cells using RNAi. Depletion of endogenous VPS4A/B to undetectable levels at 48 h after siRNA transfection (Supplementary Fig. 3b) substantially reduced the amount of CHMP4B-LAP at the midbody (Fig. 2c, and Supplementary Fig. 3c). FRAP experiments revealed that under this condition, CHMP4B-LAP turnover at the midbody was almost completely suppressed (Fig. 2e, f). We considered that this phenotype may arise from the strong reduction of the cytoplasmic CHMP4B concentration, owing to the accumulation of ESCRT-III at endosomes upon complete VPS4 depletion[47,48] (Fig. 3c, d). However, partial depletion of VPS4A/B at 20 h after siRNA transfection also reduced the fluorescence recovery after photobleaching (Fig. 2e, f) without altering the cytoplasmic CHMP4B-LAP concentration (Fig. 2c, d). The cytoplasmic levels of CHMP2B-LAP or CHMP3-LAP were also not affected upon partial VPS4A/B depletion (Supplementary Fig. 3d, e). Furthermore, microinjection of recombinant human CHMP4B protein into telophase cells resulted in rapid accumulation at the midbody in control cells, but a much slower rate in VPS4A/B-depleted cells (Supplementary Fig. 4). Together, these experiments show that VPS4 is required for dynamic turnover of ESCRT-III at the midbody.

VPS4 is required for constriction of the intercellular bridge

We next studied how VPS4 contributes to abscission. RNAi depletion of VPS4A/B delayed abscission and frequently caused cleavage furrow regression (Fig. 3a, b). These abscission failures did not occur in cells stably expressing murine VPS4B-LAP, which is resistant to siRNA targeting human VPS4A/B (Fig. 3b, and Supplementary Fig. 3a), validating that this phenotype is caused by on-target depletion. To gain further insight into the underlying defect, we investigated the ultrastructure of intercellular bridges in cryo-immobilized telophase cells. Most of the control cells contained constriction zones adjacent to the midbody with regularly spaced 17 nm diameter filaments and compressed bundles of microtubules (Fig. 3c; 4 out of 7 cells), as previously observed[4]. After partial VPS4A/B depletion at 26 h after siRNA transfection, only a small fraction of cells had 17 nm filaments (Fig. 3d; 4 out of 27 cells), and narrow constriction zones were never observed. Together, these data indicate that VPS4 is required for the formation and constriction of a functional ESCRT-III apparatus at intercellular bridges.

Vps2 and Vps24 inhibit Snf7 polymerization *in vitro*

The high ESCRT-III dynamics in cells prompted us to dissect the specific contribution of each subunit *in vitro*. As purified human ESCRT-III proteins are difficult to spontaneously polymerize on flat membranes under physiological concentrations[49], we considered to use the evolutionarily conserved budding yeast proteins. We first tested whether budding yeast Snf7 (homolog of human CHMP4) can in principle recapitulate the cellular dynamics observed for human proteins and therefore expressed a LAP-tagged version in HeLa cells. Budding yeast Snf7-LAP specifically localized to the midbody during abscission and rapidly recovered after photobleaching similar to human and mouse CHMP4B-LAP (Supplementary Fig. 5a-d), validating the use of yeast proteins for *in vitro* analysis of ESCRT-III dynamics.

Previous work showed that Snf7 spontaneously polymerizes on membrane covered areas of coverslips to form large patches composed of densely packed filament spirals[43]. We studied patch growth kinetics only in central areas of membrane-covered regions, as patches stop growth at the edge of membrane-covered regions (Supplementary Fig. 5e-g). We first investigated how Vps24 (homolog of human CHMP3) and Vps2 (CHMP2) affected the kinetics of Snf7 polymerization. We therefore incubated supported lipid bilayers with fluorescently labeled Snf7 until patches formed and then simultaneously added Vps2 and Vps24 (Fig. 4a, b, and Supplementary Video 4; 22 min). Following rapid binding, Vps2 and Vps24 suppressed patch growth and strongly reduced further accumulation of Snf7 in patches (Fig. 4c, d, and Supplementary Fig. 6a-c). Sequential injection of Vps2 and Vps24 into the fluid chamber further showed that these subunits depend on each other in their Snf7 growth-inhibitory function (Fig. 4e, Supplementary Fig. 6d, e, and Supplementary Videos 5 and 6). Thus, prolonged phases of ESCRT-III assembly, as observed during cytokinetic abscission[4,5], are not recapitulated by mixed solutions of Snf7, Vps2, and Vps24.

The inhibition of Snf7 patch growth by Vps2/Vps24 could be caused by lower rates of Snf7 subunit accumulation or by an increase of the Snf7 dissociation rate. To investigate this, we incubated supported lipid bilayers with fluorescently labeled Snf7 until patches formed and then washed out soluble Snf7. We subsequently added fluorescently labeled Vps2 and Vps24, which enriched at the edge of the patch, where newly growing Snf7 filament spirals localize[43] (Fig. 4f, g, and Supplementary Video 7). Snf7 remained stably bound to patches throughout the entire imaging period, indicating that Snf7 polymers have extremely low intrinsic subunit dissociation rates irrespective of their association with Vps2 and Vps24. The inhibition of Snf7 patch growth imposed by Vps2 and Vps24 is thus independent of Vps4 and caused by a reduced rate of Snf7 subunit incorporation.

Vps2 and Vps24 form filament bundles with Snf7

We next investigated if growth inhibition by Vps2 and Vps24 could arise from an ultrastructural change in ESCRT-III polymers. Transmission electron microscopy showed that Snf7 alone polymerized on liposomes to form one-start spirals containing a single 4.5 nm wide filament, which occasionally paired between neighboring turns (Fig. 5a, b), as previously observed[43]. When Vps2 and Vps24 were added after Snf7 polymerization, filaments appeared double-stranded and neighboring spiral turns occasionally bundled to form quadruple strands with an approximate width of 15 nm (Fig. 5c, d) – close to the width of ESCRT-III-dependent filaments observed at the abscission site in vertebrate cells[4] (Fig. 5c-f; compare Fig. 3c). Given the one-start single-stranded geometry of Snf7 spirals prior to addition of Vps2/Vps24, the paired filaments likely represent lateral copolymers of Vps2/Vps24 along Snf7.

To further characterize the morphological changes of Snf7 filaments upon addition of Vps2/24, we visualized ESCRT-III assemblies by high-speed atomic force microscopy (HS-AFM) (Fig. 5g). Snf7 alone formed spirals with pronounced filaments, but subsequent addition of Vps2/Vps24 induced a compact disc-like morphology (Fig. 5g-i). This is consistent with a filament thickening and bundling limiting access of the AFM tip in between neighboring spiral turns. Together, these data suggest that Vps2/Vps24 might reduce the rate of Snf7 polymerization through the formation of bundled filaments.

Vps4 induces subunit turnover and net growth of ESCRT-III assemblies in vitro

In cells, Vps2 and Vps24 are both present in the cytoplasm, raising the question of how ESCRT-III polymerization is sustained over prolonged periods. Our *in vivo* observations imply the possibility that Vps4 might leverage Vps2/Vps24-mediated growth inhibition by ESCRT-III turnover. To explore whether Vps4 promotes ESCRT-III turnover *in vitro*, we separately measured ESCRT-III subunit association and dissociation kinetics. We first determined the rate by which Vps4 disassembles Snf7 patches in the absence of Vps2 and Vps24. We polymerized Snf7 on supported lipid membranes, washed out soluble Snf7, and then added Vps4 and ATP. This did not cause detectable disassembly of Snf7 patches even at very high Vps4 concentrations (Fig. 6a, b), indicating that Vps4-mediated Snf7 depolymerization strictly depends on Vps2/Vps24, as shown before[37]. We thus quantified the rate of Vps4-mediated ESCRT-III patch disassembly in presence of Vps2 and Vps24. We first polymerized Snf7 patches on supported lipid membranes, then removed the soluble pool of Snf7, and subsequently added a mix of fluorescently labeled Vps2 and unlabeled Vps24, Vps4, and ATP. Vps2 first bound to Snf7 patches and subsequently partially disassembled together with Snf7 (Fig. 6c, d, Supplementary Fig. 7a, b, and Supplementary Video 8). Thus, Vps4-mediated Snf7 depolymerization is fast enough to account for dynamic turnover of its homolog CHMP4B at the midbody in human cells.

To characterize the Snf7-disassembly process at the molecular level, we visualized morphological changes of individual ESCRT-III spirals by HS-AFM. We polymerized Snf7 patches on supported lipid bilayers, then added Vps2 and Vps24, and subsequently washed out the soluble components. We then added Vps4 and ATP and acquired HS-AFM movies, which showed that ESCRT-III spirals reduced their diameter (Fig. 6e, f, and Supplementary Video 9). When omitting ATP from the reaction, Vps4 did not disassemble ESCRT-III spirals (Fig. 6g, and Supplementary Video 10), confirming that ESCRT-III disassembly is an energy-consuming process. Given that the ESCRT-III spirals did not depolymerize below a certain diameter, these data suggest that Vps4 mediates Snf7 filament disassembly predominantly from the outer regions of spirals, whereby inner spiral segments are refractory to disassembly.

We next tested whether Vps4 can mediate Snf7 turnover *in vitro*. For this purpose, we used Snf7 subunits labeled with two distinct fluorophores. We first incubated supported lipid bilayers with AlexaFluor-488-labeled Snf7 until patches formed and then added Vps24 and Vps2 to inhibit further patch growth (Fig. 7a-c, see 0 - 45 min, and Supplementary Video 11). We then exchanged the soluble pool of Snf7-AlexaFluor-488 with Snf7-Atto-647N while maintaining Vps2 and Vps24 in the reaction. At this point, we also added Vps4. Snf7 polymer patches maintained constant size and did not incorporate Atto-647N-Snf7, presumably because ATP was not yet present (Fig. 7a-c, see 45 - 54 min). Indeed, subsequent ATP addition caused dissociation of AlexaFluor-488-Snf7 from patches, but also concomitant binding of Atto-647N-Snf7 (Fig. 7a-c, see 54 - 88 min). Thus, an ATP-dependent activity of Vps4 promotes not only disassembly of ESCRT-III but also the formation of new ESCRT-III polymers on membranes.

Interestingly, Vps4 and ATP also restored the macroscopic growth of Snf7 patches despite the continued presence of Vps2 and Vps24 (Fig. 7a, b, see 58 - 88 min, and Supplementary Video 11). We thus tested if a solution containing Vps4, ATP, and all three ESCRT-III subunits supports nucleation and growth of ESCRT-III polymers as observed *in vivo*. Strikingly, this combination resulted in efficient nucleation and growth of ESCRT-III patches, in contrast to a mix that lacked Vps4 (Fig. 7d, e). Furthermore, the net ESCRT-III assembly rate increased with higher concentrations of Vps4 (Supplementary Fig. 7c). Thus, Vps4 promotes net growth of ESCRT-III assemblies in presence of growth-inhibiting Vps2 and Vps24 subunits.

Vps4 induces dynamic growth and shrinkage of ESCRT-III filament spirals

To study Vps4-mediated polymer remodeling at the molecular level, we visualized ESCRT-III spirals by HS-AFM. We assembled Snf7 spirals on supported lipid bilayers and then added Vps2, Vps24, Vps4, and ATP. This induced a drastic reorganization of ESCRT-III polymers: preexisting spirals reduced their size, while many new spirals nucleated and grew in between the original spirals (Fig. 8a, b, and Supplementary Video 12). The innermost parts of ESCRT-III spirals appeared refractory to disassembly and thus might represent the stably-bound fraction of ESCRT-III observed by fluorescence microscopy. In contrast, pre-existing spirals remained unchanged in the absence of ATP (Fig. 8c, and Fig. 6g). Thus, Vps4 induces a dynamic steady-state with both growing and shrinking ESCRT-III spirals when Snf7, Vps2, Vps24 are present in solution.

Furthermore, while ESCRT-III spirals formed an immobile array in the absence of ATP, the addition of ATP induced substantial lateral mobility of individual ESCRT-III spirals relative to each other (Fig. 8d-f, and Fig. 6g). Thus, in the presence of Vps4 and ATP, ESCRT-III forms highly dynamic polymer structures on membranes.

DISCUSSION

Our study shows that membrane-bound ESCRT-III polymers rapidly turn over subunits with cytoplasmic pools while they assemble into larger structures. The dynamic subunit turnover is driven by Vps4 and is necessary to sustain efficient net growth of ESCRT-III assemblies in presence of inhibitory Vps2 and Vps24 subunits.

Most previous models for ESCRT-III-mediated membrane fission imply sequential recruitment of different ESCRT-III subunits and Vps4 to establish distinct phases of polymer growth, reorganization/maturation, and disassembly[5,14,18-21,23-25,28,30,31]. However, our study shows that different ESCRT-III subunits and VPS4 accumulate at the midbody with indistinguishable kinetics. This does not rule out sequential subunit binding at the single-filament level, but indicates that the distinct stages of ESCRT-III accumulation, constriction, and disassembly during abscission cannot be explained by a sequence of subunit binding.

Our findings call for re-interpretation of the terminal phenotype resulting from Vps4 depletion – the accumulation of ESCRT-III polymers in endosomes (termed class E compartment in yeast) that has led to the model of Vps4 serving predominantly as a disassembly factor [26,28,33,50]. We show that Vps4 is important for efficient ESCRT-III assembly, yet we also note that residual slow ESCRT-III polymerization in the absence of Vps4 is sufficient to ultimately capture all cytoplasmic subunits in class E compartments – owing to the extremely low intrinsic subunit dissociation rates.

At the molecular level, Vps4 might promote the net growth of ESCRT-III assemblies by constant turnover of Vps2 and Vps24 in side-by-side co-polymers along Snf7 filaments – to create growthcompetent free Snf7 filament tips (Fig. 8g). Furthermore, Vps4 might induce subunit turnover at the core of ESCRT-III filament bundles, in analogy to interaction of the Vps4 homolog Spastin with the lattice of microtubules[51] (Fig. 8g). In contrast to previous models[5,52], however, Vps4 does not cut an ESCRT-III helix during a single definite time point to induce tension release, but rather continuously remodels filaments. Within bundled filaments, such turnover does not necessarily lead to a complete breakage of larger structures.

The innermost parts of ESCRT-III spirals appear refractory to disassembly even at high concentrations of Vps4, suggesting that ESCRT-III interaction with Vps4 might depend on mechanical stress owing to low filament curvature or on filament polarity. Potential stochastic fluctuations in subunit turnover rates could then lead to dynamic growth and shrinkage of ESCRT-III spirals.

Vps4-induced subunit turnover in ESCRT-III assemblies might directly contribute to membrane constriction. Indeed, macroscopic shape changes of many other cellular polymer structures critically depend on dynamic subunit turnover within the constituent filaments, as for example mitotic spindles[53] or actomyosin rings[54]. In ESCRT-III assemblies, Vps4-induced subunit turnover might facilitate sliding of adjacent helix turns, thereby promoting constriction of mechanically pre-stressed, low-curved filaments into more relaxed high-curvature states[43]. The underlying bending forces could be generated by binding of Vps2 and Vps24 to Snf7[41], or by shortening-induced increase of filament rigidity. By revealing dynamic subunit turnover in ESCRT-III assemblies, our study provides a framework for understanding how this highly conserved membrane fission machinery adapts to diverse membrane geometries.

ACKNOWLEDGMENTS

D.W.G. has received financial support from the European Community's Seventh Framework Programme FP7/2007-2013 under grant agreements no 241548 (MitoSys) and no 258068 (Systems Microscopy), from an ERC Starting Grant (agreement no 281198), from the Wiener Wissenschafts-, Forschungs- und Technologiefonds (WWTF; project nr. LS14-009), and from the Austrian Science Fund (FWF; project nr. SFB F34-06). B.E.M. has received a PhD fellowship from the Boehringer Ingelheim Fonds. A.R. acknowledges funding from: Human Frontier Science Program (HFSP), Young Investigator Grant #RGY0076-2008: the European Research Council (ERC), starting (consolidator) grant #311536-MEMFIS: the Swiss National Fund for Research, grants #131003A_130520 and #131003A_149975. NC acknowledges the European Commission for the Marie-Curie post-doctoral fellowship CYTOCUT #300532-2011. J.M.F. acknowledges funding by an EMBO long-term fellowship (ALTF 1065-2015). T.M.R. has received funding from the Deutsche Forschungsgemeinschaft (DFG) grant MU1423/4-1. S.S.

acknowledges funding by an ANR grant ANR-Nano (ANR-12-BS10-009-01) and a European Research Council (ERC) Starting Grant (#310080, MEM-STRUCT-AFM). The authors thank D. Teis, M. Alonso Y Adell, C. Campsteijn, and J. Gruenberg for comments on the manuscript, the IMBA/IMP/GMI BioOptics core facility for technical support, the EM Facility of the Vienna Biocenter Core Facilities (VBCF), who performed parts of the sample preparation and electron microscopy, F. Humbert for protein purification, C. Sommer and R. Höfler for statistical advice, C. Blaukopf for technical support, W. Reiter for providing *S. cerevisiae* genomic DNA, and Life Science Editors for editing assistance.

AUTHOR CONTRIBUTIONS

B.E.M. designed, conducted, and analyzed all cell biological experiments, and analyzed part of the HS-AFM data. N.C. designed, conducted, and analyzed in vitro reconstitution experiments based on fluorescence microscopy. L.R-M. designed, conducted, and analyzed HS-AFM experiments. J.M-v-F. and N.C. designed, conducted, and analyzed electron microscopy of in vitro-assembled ESCRT-III polymers. J.K. and T.M-R designed, conducted, and analyzed electron microscopy experiments of intercellular bridges. J.L. established the CHMP4B purification and produced labelled CHMP4B. I.P. generated HeLa cells stably expressing mmVPS4B-LAP. B.E.M., N.C., D.W.G., A.R. and S.S. conceived the project, analyzed data, and wrote the manuscript.

COMPETING FINANCIAL INTERESTS

The authors declare no competing financial interests. Correspondence and requests for materials should be addressed to D.W.G. (daniel.gerlich@imba.oeaw.ac.at) or A.R (aurelien.roux@unige.ch).

REFERENCES

1 Hurley, J. H. ESCRTs are everywhere. *EMBO J* **34**, 2398-2407 (2015).

2 Hanson, P. I. & Cashikar, A. Multivesicular body morphogenesis. *Annu Rev Cell Dev Biol* **28**, 337-362 (2012).

3 Carlton, J. G. & Martin-Serrano, J. Parallels between cytokinesis and retroviral budding: a role for the ESCRT machinery. *Science* **316**, 1908-1912 (2007).

4 Guizetti, J. *et al.* Cortical constriction during abscission involves helices of ESCRT-III-dependent filaments. *Science* **331**, 1616-1620 (2011).

5 Elia, N., Sougrat, R., Spurlin, T. A., Hurley, J. H. & Lippincott-Schwartz, J. Dynamics of endosomal sorting complex required for transport (ESCRT) machinery during cytokinesis and its role in abscission. *Proc Natl Acad Sci U S A* **108**, 4846-4851 (2011).

6 Lafaurie-Janvore, J. *et al.* ESCRT-III assembly and cytokinetic abscission are induced by tension release in the intercellular bridge. *Science* **339**, 1625-1629 (2013).

7 Mierzwa, B. & Gerlich, D. W. Cytokinetic abscission: molecular mechanisms and temporal control. *Dev Cell* **31**, 525-538 (2014).

8 Vietri, M. *et al.* Spastin and ESCRT-III coordinate mitotic spindle disassembly and nuclear envelope sealing. *Nature* **522**, 231-235 (2015).

9 Olmos, Y., Hodgson, L., Mantell, J., Verkade, P. & Carlton, J. G. ESCRT-III controls nuclear envelope reformation. *Nature* **522**, 236-239 (2015).

10 Raab, M. *et al.* ESCRT III repairs nuclear envelope ruptures during cell migration to limit DNA damage and cell death. *Science* **352**, 359-362 (2016).

11 Denais, C. M. *et al.* Nuclear envelope rupture and repair during cancer cell migration. *Science* **352**, 353-358 (2016).

12 Jimenez, A. J. *et al.* ESCRT machinery is required for plasma membrane repair. *Science* **343**, 1247136 (2014).

13 von Schwedler, U. K. *et al.* The protein network of HIV budding. *Cell* **114**, 701-713 (2003).

14 Bleck, M. *et al.* Temporal and spatial organization of ESCRT protein recruitment during HIV-1 budding. *Proc Natl Acad Sci U S A* **111**, 12211-12216 (2014).

15 Baietti, M. F. *et al.* Syndecan-syntenin-ALIX regulates the biogenesis of exosomes. *Nat Cell Biol* **14**, 677-685 (2012).

16 Choudhuri, K. *et al.* Polarized release of T-cell-receptor-enriched microvesicles at the immunological synapse. *Nature* **507**, 118-123 (2014).

17 Matusek, T. *et al.* The ESCRT machinery regulates the secretion and long-range activity of Hedgehog. *Nature* **516**, 99-103 (2014).

18 Henne, W. M., Stenmark, H. & Emr, S. D. Molecular mechanisms of the membrane sculpting ESCRT pathway. *Cold Spring Harb Perspect Biol* **5** (2013).

19 McCullough, J., Colf, L. A. & Sundquist, W. I. Membrane fission reactions of the mammalian ESCRT pathway. *Annu Rev Biochem* **82**, 663-692 (2013).

20 Peel, S., Macheboeuf, P., Martinelli, N. & Weissenhorn, W. Divergent pathways lead to ESCRT-III-catalyzed membrane fission. *Trends Biochem Sci* **36**, 199-210 (2011).

21 Hurley, J. H. & Hanson, P. I. Membrane budding and scission by the ESCRT machinery: it's all in the neck. *Nat Rev Mol Cell Biol* **11**, 556-566 (2010).

22 Guizetti, J. & Gerlich, D. W. ESCRT-III polymers in membrane neck constriction. *Trends Cell Biol* **22**, 133-140 (2012).

23 Schmidt, O. & Teis, D. The ESCRT machinery. *Curr Biol* **22**, R116-120 (2012).

24 Schoneberg, J., Lee, I. H., Iwasa, J. H. & Hurley, J. H. Reverse-topology membrane scission by the ESCRT proteins. *Nat Rev Mol Cell Biol* **18**, 5-17 (2017).

25 Christ, L., Raiborg, C., Wenzel, E. M., Campsteijn, C. & Stenmark, H. Cellular Functions and Molecular Mechanisms of the ESCRT Membrane-Scission Machinery. *Trends Biochem Sci* **42**, 42-56 (2017).

26 Babst, M., Katzmann, D. J., Estepa-Sabal, E. J., Meerloo, T. & Emr, S. D. Escrt-III: an endosome-associated heterooligomeric protein complex required for mvb sorting. *Dev Cell* **3**, 271-282 (2002).

27 Samson, R. Y., Obita, T., Freund, S. M., Williams, R. L. & Bell, S. D. A role for the ESCRT system in cell division in archaea. *Science* **322**, 1710-1713 (2008).

28 Teis, D., Saksena, S. & Emr, S. D. Ordered assembly of the ESCRT-III complex on endosomes is required to sequester cargo during MVB formation. *Dev Cell* **15**, 578-589 (2008).

29 Teis, D., Saksena, S., Judson, B. L. & Emr, S. D. ESCRT-II coordinates the assembly of ESCRT-III filaments for cargo sorting and multivesicular body vesicle formation. *EMBO J* **29**, 871-883 (2010).

30 Saksena, S., Wahlman, J., Teis, D., Johnson, A. E. & Emr, S. D. Functional reconstitution of ESCRT-III assembly and disassembly. *Cell* **136**, 97-109 (2009).

31 Wollert, T., Wunder, C., Lippincott-Schwartz, J. & Hurley, J. H. Membrane scission by the ESCRT-III complex. *Nature* **458**, 172-177 (2009).

32 Carlson, L. A. & Hurley, J. H. In vitro reconstitution of the ordered assembly of the endosomal sorting complex required for transport at membrane-bound HIV-1 Gag clusters. *Proc Natl Acad Sci U S A* **109**, 16928-16933 (2012).

33 Babst, M., Wendland, B., Estepa, E. J. & Emr, S. D. The Vps4p AAA ATPase regulates membrane association of a Vps protein complex required for normal endosome function. *EMBO J* **17**, 2982-2993 (1998).

34 Obita, T. *et al.* Structural basis for selective recognition of ESCRT-III by the AAA ATPase Vps4. *Nature* **449**, 735-739 (2007).

35 Stuchell-Brereton, M. D. *et al.* ESCRT-III recognition by VPS4 ATPases. *Nature* **449**, 740-744 (2007).

36 Lata, S. *et al.* Helical structures of ESCRT-III are disassembled by VPS4. *Science* **321**, 1354-1357 (2008).

37 Adell, M. A. *et al.* Coordinated binding of Vps4 to ESCRT-III drives membrane neck constriction during MVB vesicle formation. *J Cell Biol* **205**, 33-49 (2014).

38 Yang, B., Stjepanovic, G., Shen, Q., Martin, A. & Hurley, J. H. Vps4 disassembles an ESCRT-III filament by global unfolding and processive translocation. *Nat Struct Mol Biol* **22**, 492-498 (2015).

39 Ghazi-Tabatabai, S. *et al.* Structure and disassembly of filaments formed by the ESCRT-III subunit Vps24. *Structure* **16**, 1345-1356 (2008).

40 Pires, R. *et al.* A crescent-shaped ALIX dimer targets ESCRT-III CHMP4 filaments. *Structure* **17**, 843-856 (2009).

41 Henne, W. M., Buchkovich, N. J., Zhao, Y. & Emr, S. D. The Endosomal Sorting Complex ESCRT-II Mediates the Assembly and Architecture of ESCRT-III Helices. *Cell* **151**, 356-371 (2012).

42 Shen, Q. T. *et al.* Structural analysis and modeling reveals new mechanisms governing ESCRT-III spiral filament assembly. *J Cell Biol* **206**, 763-777 (2014).

43 Chiaruttini, N. *et al.* Relaxation of Loaded ESCRT-III Spiral Springs Drives Membrane Deformation. *Cell* **163**, 866-879 (2015).

44 McCullough, J. *et al.* Structure and membrane remodeling activity of ESCRT-III helical polymers. *Science* **350**, 1548-1551 (2015).

45 McMillan, B. J. *et al.* Electrostatic Interactions between Elongated Monomers Drive Filamentation of Drosophila Shrub, a Metazoan ESCRT-III Protein. *Cell Rep* **16**, 1211-1217 (2016).

46 Hanson, P. I., Roth, R., Lin, Y. & Heuser, J. E. Plasma membrane deformation by circular arrays of ESCRT-III protein filaments. *J Cell Biol* **180**, 389-402 (2008).

47 Cashikar, A. G. *et al.* Structure of cellular ESCRT-III spirals and their relationship to HIV budding. *Elife* **3** (2014).

48 Babst, M., Sato, T. K., Banta, L. M. & Emr, S. D. Endosomal transport function in yeast requires a novel AAA-type ATPase, Vps4p. *EMBO J* **16**, 1820-1831 (1997).

49 Lee, I. H., Kai, H., Carlson, L. A., Groves, J. T. & Hurley, J. H. Negative membrane curvature catalyzes nucleation of endosomal sorting complex required for transport (ESCRT)-III assembly. *Proc Natl Acad Sci U S A* **112**, 15892-15897 (2015).

50 Cashikar, A. G. *et al.* Structure of cellular ESCRT-III spirals and their relationship to HIV budding. *Elife*, e02184 (2014).

51 Roll-Mecak, A. & Vale, R. D. Structural basis of microtubule severing by the hereditary spastic paraplegia protein spastin. *Nature* **451**, 363-367 (2008).

52 Elia, N., Fabrikant, G., Kozlov, M. M. & Lippincott-Schwartz, J. Computational model of cytokinetic abscission driven by ESCRT-III polymerization and remodeling. *Biophys J* **102**, 2309-2320 (2012).

53 Kline-Smith, S. L. & Walczak, C. E. Mitotic spindle assembly and chromosome segregation: refocusing on microtubule dynamics. *Mol Cell* **15**, 317-327 (2004).

54 Pollard, T. D., Blanchoin, L. & Mullins, R. D. Molecular mechanisms controlling actin filament dynamics in nonmuscle cells. *Annu Rev Biophys Biomol Struct* **29**, 545-576 (2000).

55 Zemp, I. *et al.* Distinct cytoplasmic maturation steps of 40S ribosomal subunit precursors require hRio2. *J Cell Biol* **185**, 1167-1180 (2009).

56 Poser, I. *et al.* BAC TransgeneOmics: a high-throughput method for exploration of protein function in mammals. *Nat Methods* **5**, 409-415 (2008).

57 Hein, M. Y. *et al.* A human interactome in three quantitative dimensions organized by stoichiometries and abundances. *Cell* **163**, 712-723 (2015).

58 Schmitz, M. H. & Gerlich, D. W. Automated live microscopy to study mitotic gene function in fluorescent reporter cell lines. *Methods Mol Biol* **545**, 113-134 (2009).

59 Lukinavicius, G. *et al.* Fluorogenic probes for live-cell imaging of the cytoskeleton. *Nat Methods* **11**, 731-733 (2014).

60 Schindelin, J. *et al.* Fiji: an open-source platform for biological-image analysis. *Nat Methods* **9**, 676-682 (2012).

61 Morita, E. *et al.* Human ESCRT-III and VPS4 proteins are required for centrosome and spindle maintenance. *Proc Natl Acad Sci U S A* **107**, 12889-12894 (2010).

62 Wollert, T. & Hurley, J. H. Molecular mechanism of multivesicular body biogenesis by ESCRT complexes. *Nature* **464**, 864-869 (2010).

63 Aguet, F., Van De Ville, D. & Unser, M. Model-based 2.5-d deconvolution for extended depth of field in brightfield microscopy. *IEEE Trans Image Process* **17**, 1144-1153 (2008).

FIGURE LEGENDS

Figure 1 | ESCRT-III assemblies at the midbody dynamically turn over subunits in early and late abscission stages. (**a**) Validation of mmCHMP4B-LAP functionality by RNAi phenotype rescue. Cumulative histograms indicate the duration from complete cleavage furrow ingression until abscission for wildtype HeLa cells and for HeLa cells expressing mmCHMP4B-LAP at 55-80 h after transfection of siRNAs (3 replicates with combined sample numbers of n = 48 for wildtype+siControl, n = 38 for wildtype+siCHMP4B, n = 60 for mmCHMP4B-LAP+siControl, and n = 46 for mmCHMP4B-LAP+siCHMP4B). siCHMP4B (hs) targets only endogenous human CHMP4B but not mmCHMP4B-LAP. (**b**) FRAP of mmCHMP4B-LAP at a HeLa cell midbody at early and late abscission stages, stained with SiR-tubulin. Dashed circles indicate photobleaching region; time 0 indicates first image after photobleaching. (**c**-**d**) Fluorescence recovery curves for (**c**) early abscission (n = 18 from 4 replicates) or (**d**) late abscission stages (n = 17 from 4 replicates). Single exponential function f(t)=1-e^(-k*t), or double exponential function f(t)=A1*(1-e^(-k1*t))+(1-A1*)(1-e^(-k2*t)) were fitted to the data. Points and shaded areas indicate mean ± SEM of fluorescence; dashed lines indicate fits of single or double exponential functions. (**e**) Quantification of highly mobile fractions by fitting double exponential functions to data from c, d. Dots represent individual cells. (**f**) 3D live-cell confocal microscopy of the intercellular bridge during telophase, in HeLa cells expressing hsCHMP2B-LAP or hsCHMP3-LAP, respectively, stained with SiR-tubulin. Arrowheads indicate abscission. (**g**) Quantification of hsCHMP2B-LAP (n = 17 from 4 replicates), hsCHMP3-LAP (n = 13 from 3 replicates), and hsCHMP4B-LAP (n = 17 from 3 replicates) accumulation at the midbody. Points and shaded areas indicate mean ± SEM; normalized to intercellular bridge fluorescence after cleavage furrow ingression, and temporally aligned to abscission (time point 0). (**h**) Highly mobile fractions of LAP-tagged ESCRT-III subunits derived from double exponential fits to FRAP curves as in c, d. Each dot represents a single FRAP experiment acquired in 3 replicates; bars indicate medians. (**i**) Residence times of highly mobile fractions for cells shown in h. Scale bars, 1 μm in b, f.

Figure 2 | VPS4 is required for ESCRT-III accumulation and turnover. (**a**) Confocal microscopy of the intercellular bridge in HeLa cells expressing mmCHMP4B-LAP or mmVPS4B-LAP, respectively, stained with SiR-tubulin. Arrowheads indicate abscission. (**b**) Midbody accumulation of mmCHMP4B-LAP (n = 15 from 3 replicates) or mmVPS4B-LAP (n = 16 from 3 replicates) relative to abscission (time point 0). Points and shaded areas indicate mean and SEM. (**c**) Live-cell images of telophase cells expressing mmCHMP4B-LAP after transfection of a non-targeting control siRNA, or siRNAs targeting hsVPSP4A/B after 20 h or 48 h. Insets show enlarged midbody regions. The same contrast settings were used for all panels. (**d**) Quantification of cytoplasmic mmCHMP4B-LAP levels from data in e, f. Dots represent individual cells from 3 replicates; bars indicate medians. (**e**) FRAP curves and double exponential fits for mmCHMP4B-LAP at pre-constriction stages transfected with control siRNAs (n = 18 from 3 replicates) or siRNAs targeting VPS4A/B (n = 18 for siVPS4A/B 20h, and n = 17 for siVPS4A/B 48h from 3 replicates). Points and shaded areas indicate mean ± SEM. (**f**) Highly mobile fractions of mmCHMP4B-LAP determined by double exponential fits to FRAP curves shown in e (3 replicates with combined sample numbers of n = 9 for siControl 48h, n = 18 for siVPS4A/B 20h, and n = 13 for siVPS4A/B 48h). Statistical test using the two-sided Kolmogorov–Smirnov test yielded $P = 6.562e^{-3}$ for siControl 48h relative to siVPS4A/B 20h, and $P = 4.021e^{-6}$ for siControl 48h relative to siVPS4A/B 48h. Dots represent individual cells; bars indicate medians. Scale bars, 1 µm in a; 5 µm or 1 µm (inset) in c.

Figure 3 | VPS4 is required for constriction of the intercellular bridge. (**a-b**) Transfection of siRNAs targeting hsVPS4A/B causes abscission failure in wild-type HeLa cells, but not in HeLa cells stably expressing mmVPS4B-LAP. (**a**) Progression from cleavage furrow ingression (time point 0) until abscission in wildtype HeLa cells at 30-50 h after transfection of indicated siRNAs (n = 84 for wildtype+siControl, and n = 80 for wildtype+siVPS4A/B for 3 fields of view from 2 replicates). (**b**) Rescue of abscission failure in HeLa cells stably expressing mmVPS4B-LAP (data from a, n = 54 for mmVPS4B-LAP+siControl, and n = 45 for mmVPS4B-LAP+siVPS4A/B). Bars and error bars indicate mean ± SEM. (**c**) Representative electron micrograph of an intercellular bridge of a control cell (n = 10, out of which 3 cells had filaments without constriction, and 4 showed filaments with constriction). Arrowheads indicate 17 nm diameter filaments. (**d**) Intercellular bridge of a cell 26 h after transfection of VPS4A/B siRNA (n = 26, out of which 4 cells showed filaments without constriction). Arrowheads indicate 17 nm diameter filaments. Scale bars, 200 nm in c, d.

Figure 4 | Vps2 and Vps24 cooperatively bind Snf7 patches and inhibit ESCRT-III polymerization. (**a**) Time-lapse microscopy of ESCRT-III polymerization on supported lipid membranes in a microfluidic flow chamber. Recombinant Snf7-AlexaFluor-488 was injected at t = 0 min; Vps2-Atto-565 and Vps24 were added at t = 22 min. (**b**) Kymograph of a single ESCRT-III patch from a. (**c-d**) Quantification of (**c**) mean fluorescence and (**d**) patch diameters from 24 patches (quantified from 4 fields of view within a representative experiment, and consistent results in 3 additional replicates using differently labeled proteins, e.g. Supplementary Fig. 6a-c). Curves and shaded areas represent mean ± SEM. (**e**) Kymograph of an experiment where Snf7-AlexaFluor-647N was added at t = 0 min, followed by sequential addition of Vps24-AlexaFluor-488 and Vps2-Atto-565 (representative image from 24 patches within the shown experiment, and one additional replicate). (**f**) Kymograph of an ESCRT-III patch, where Snf7-AlexaFluor-488 was added at t = 0 min, then washed out during 28-32 min (shaded area), followed by addition of Vps2-Atto-565 and Vps24 at t = 47 min. The transient increase of Vps2 signal during washout resulted from background ambient light. (**g**) Fluorescence quantification of 37 patches (analyzed from 4 fields of view within the shown experiment, and 3 additional replicates). Curves and shaded areas represent mean ± SEM. Scale bars, 5 µm in a; 5 µm (vertical) and 5 min (horizontal) in b, e, f.

Figure 5 | Vps2 and Vps24 polymerize side-by-side with Snf7 to form filament bundles. (**a**) Transmission electron microscopy of Snf7 spirals polymerized on liposomes. Colored overlays indicate the number of parallel filament strands. (**b**) Distribution of filament bundle lengths quantified in 11 spirals (from 3 replicates). (**c**) Snf7 was polymerized on liposomes, followed by Vps2 and Vps24 addition. Colored overlays indicate the number of parallel filament strands. (**d**) Quantification of 17 spirals (from 2 replicates). (**e**) Examples of filament morphologies with different strand numbers, corresponding to colored overlays used in a-d. (**f**) Averaged line profiles across ESCRT-III filament bundles from a-d (n = 3 for 1 strand, n = 8 for 2 strands, n = 3 for 3 strands, n = 8 for 4 strands; and n = 3 for 6 strands). Curves and shaded areas indicate mean ± SEM. (**g-i**) HS-AFM imaging of ESCRT-III polymers on supported lipid membranes. Snf7 was polymerized on lipid membranes, followed by addition of Vps2 and Vps24 at t = 0. (**g**) Spiral morphology before and after addition of Vps2 and Vps24. Green and magenta lines indicate line profiles used to (**h**) measure height variability. (**i**) Height variability was measured as coefficient of variation along radial line profiles within spirals before and after addition of Vps2 and Vps24, respectively, as shown in g, h (n = 28 for Snf7, and n= 26 for Snf7+Vps2+Vps24 from 2 replicates). Statistical test using the two-sided Kolmogorov–Smirnov test yielded P = 2.875e-14 for Snf7 relative to Snf7+Vps2+Vps24. Dots represent individual line profile measurements; bars indicate medians. Scale bars, 50 nm in a, c, e; 200 nm in g.

Figure 6 | Kinetics of ESCRT-III patch disassembly by Vps4. (**a**) Kymograph of a representative patch from time-lapse microscopy of Snf7 patches on supported lipid membranes in a flow chamber. A solution of Snf7-AlexaFluor-488 was injected into the flow chamber and incubated until patches polymerized on the membrane. Snf7 was washed out at t = 22 min, followed by addition of ATP and 8 µM Vps4 at t = 33 min. (**b**) Quantification of mean fluorescence of 13 patches as in a (4 different fields of view within the shown experiment, and one additional replicate). Curves and shaded areas indicate mean ± SEM. (**c**) A solution of Snf7-AlexaFluor-488 was injected into the flow chamber and incubated until patches polymerized. At t = 34 min, Snf7 was removed from the solution and Vps2-Atto-565, Vps24, Vps4, and ATP were injected. (**d**) Quantification of mean fluorescence of 33 patches from c (4 fields of view within the shown experiment, and one additional replicate). Curves and shaded areas indicate mean ± SEM. (**e-g**) Vps4-induced dynamic turnover and lateral mobility of ESCRT-III filament spirals depends on ATP. (**e**) HS-AFM imaging of ESCRT-III spirals. Assemblies were generated by polymerization of Snf7 on supported lipid membranes, followed by addition of Vps2 and Vps24. After washout of all soluble components, Vps4 was injected. Then, ATP and Mg^{2+} were added, and imaging was started 22 s later (t = 0). Images represent averages of 2 consecutive time frames to improve signal-to-noise ratio. (**f**) Quantification of spiral diameters from f (119 spirals from a representative experiment, out of 6 independent replicates). Dots represent single spirals; bars indicate medians. (**g**) Snf7 was polymerized on supported lipid membranes, followed by addition of Vps2 and Vps24, and subsequent addition of Vps4, as in Fig. 8a but without ATP. Imaging was started 30 s after addition of Vps4 (t = 0). Images represent averages of 3 consecutive time frames. Corresponding spiral diameter quantification is shown in Fig. 8c. Scale bars, 5 µm (vertical) and 5 min (horizontal) in a, c; 100 nm in e; 200 nm in g.

Figure 7 | Vps4 induces subunit turnover and net growth of ESCRT-III assemblies. (**a**) Time-lapse microscopy of ESCRT-III polymerization on supported lipid membranes. Snf7-AlexaFluor-488 was injected at t = 0 min. Vps2-Atto-565 and Vps24 were added at t = 36 min while maintaining Snf7 in the solution. At t = 45 min, Snf7-AlexaFluor-488 was removed and a mix containing Snf7-Atto-647N, Vps2-Atto-565, Vps24 and Vps4 was added, followed by addition of ATP at t = 54 min. (**b**) Kymograph of a single patch from a. (**c**) Mean fluorescence quantification of 35 patches (4 fields of view within the shown experiment, and consistent results in 2 additional replicates using differently labeled proteins). Curves and shaded areas represent mean ± SEM. (**d-e**) Time-lapse microscopy of in vitro polymerization as in a, but for a mixed solution containing Snf7-AlexaFluor-488, Vps2-Atto-565, Vps24, and ATP (**d**) in the presence of Vps4, or (**e**) without Vps4. Representative images of 2 replicates per condition are shown. Scale bars, 10 μm in a, d, e; 5 μm (vertical) and 5 min (horizontal) in b.

Figure 8 | Vps4 induces dynamic reorganization of ESCRT-III assemblies. HS-AFM imaging of ESCRT-III polymers on supported lipid membranes. (**a**) Snf7 was polymerized on supported lipid membranes, followed by addition of Vps2, Vps24, and Vps4. Then, Mg^{2+} and ATP were added and imaging was started 5.5 min later (t = 0). Overlays highlight pre-formed spirals (blue) or newly formed spirals (orange). Bottom panels show a close-up of the nucleation of a new spiral. Images represent averages of 3 consecutive time frames to improve the signal-to-noise ratio. Scale bars, 200 nm (top panel) or 5 nm (bottom panel). (**b**) Quantification of spiral diameters from a (274 spirals from a representative experiment, out of 3 independent replicates). Dots represent single spirals; bars indicate medians. (**c**) Quantification of spiral diameters from Fig. 6g (175 spirals from a representative experiment, from a total of 6 independent replicates). Dots represent single spirals; bars indicate medians. (**d**) Tracking of spiral centers from a. (**e**) Tracking as in d, but for an experiment without ATP and Mg^{2+} as shown in Fig. 6g. (**f**) Quantification of mean velocity of spiral centers from d, e (n = 34 for with ATP, and n = 31 for without ATP). Statistical test using the two-sided Kolmogorov–Smirnov test yielded P = 4.441e-16 for spiral velocities in the presence of ATP relative to velocities in the absence of ATP. Dots represent single tracks; bars indicate medians. (**g**) Model of dynamic ESCRT-III assembly and constriction. Vps4 mediates continuous subunit turnover in ESCRT-III assemblies during growth and constriction. (1) At the tip, dynamic turnover of growth-inhibitory Vps2 and Vps24 subunits could sustain extension of inward-curving filaments. (2) At the core of filament bundles, Vps4-mediated subunit turnover could facilitate sliding of neighboring helical turns to promote constriction.

SUPPLEMENTARY INFORMATION

Supplementary Information includes:

Supplementary Figures 1-8

Supplementary Videos 1-12

Mierzwa et al., Fig. 1

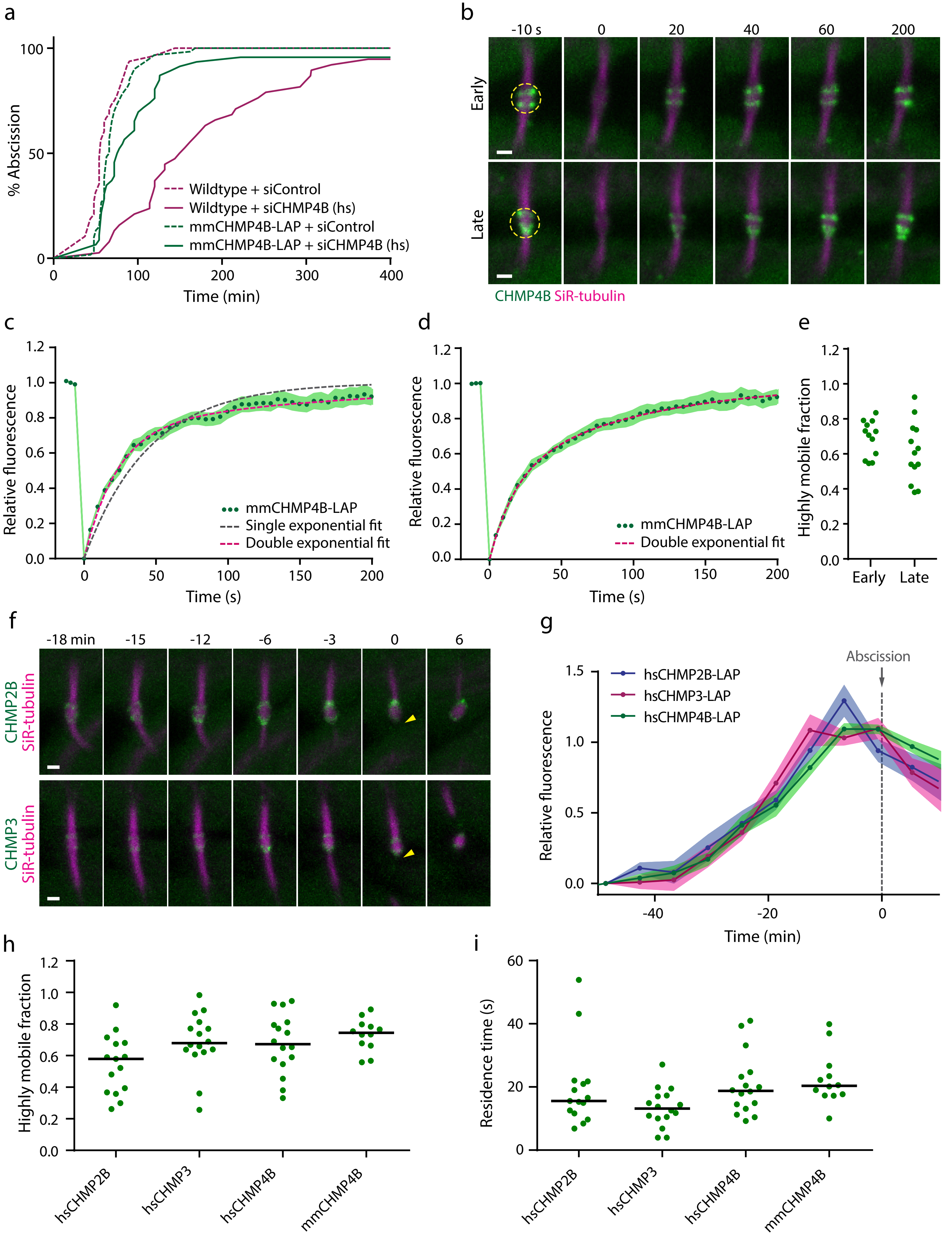

Mierzwa et al., Fig. 2

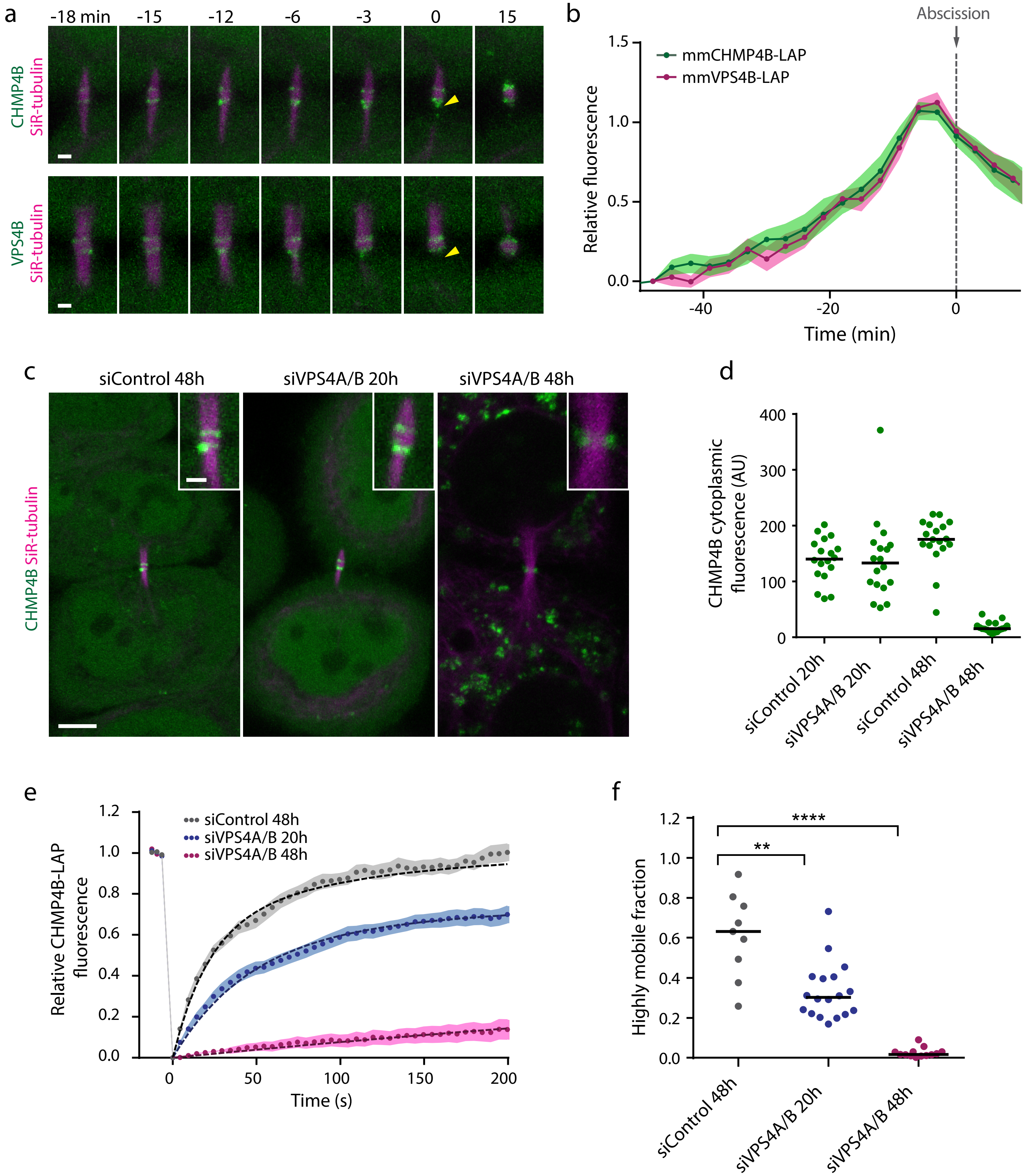

Mierzwa et al., Fig. 3

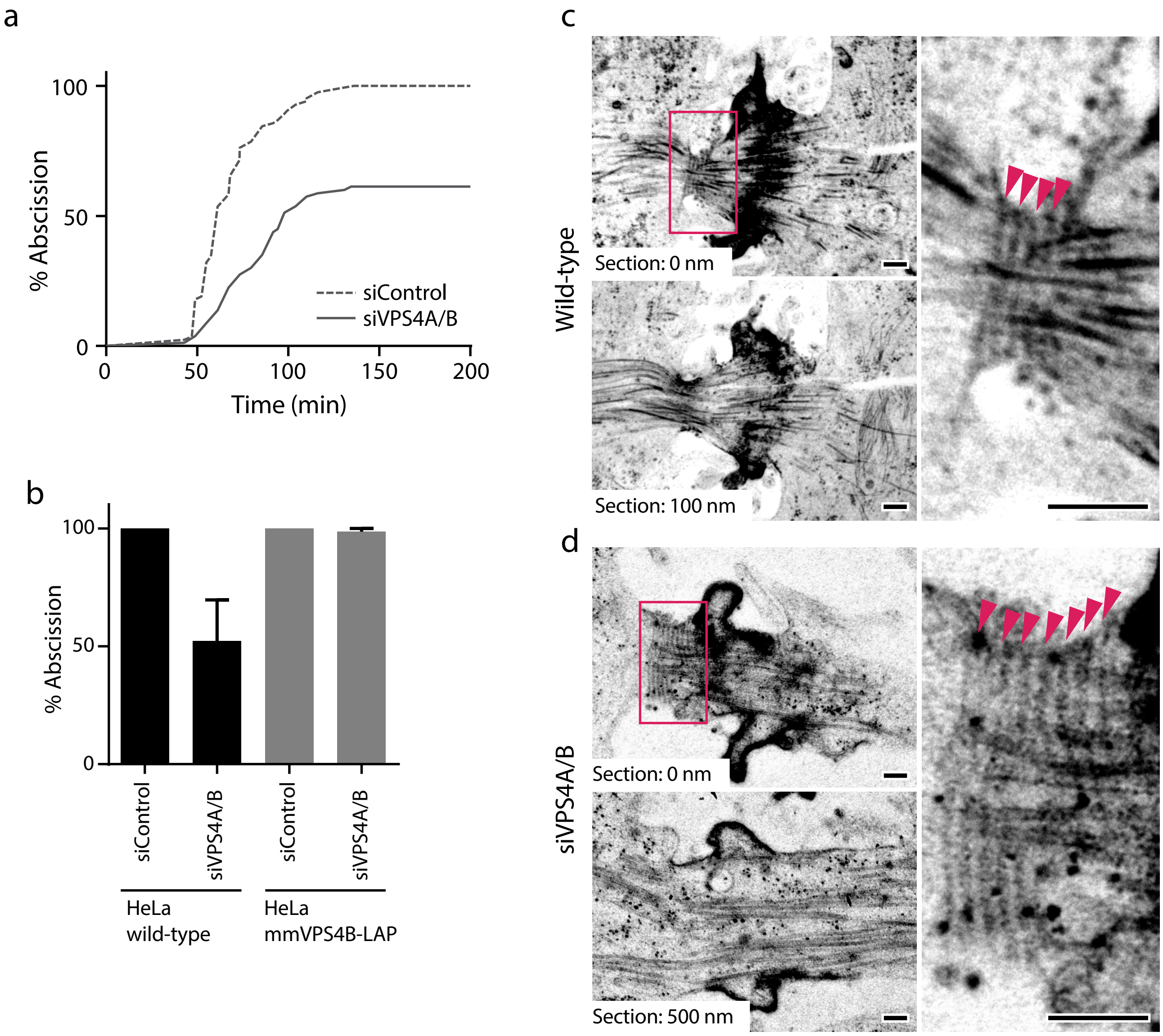

Mierzwa et al., Fig. 4

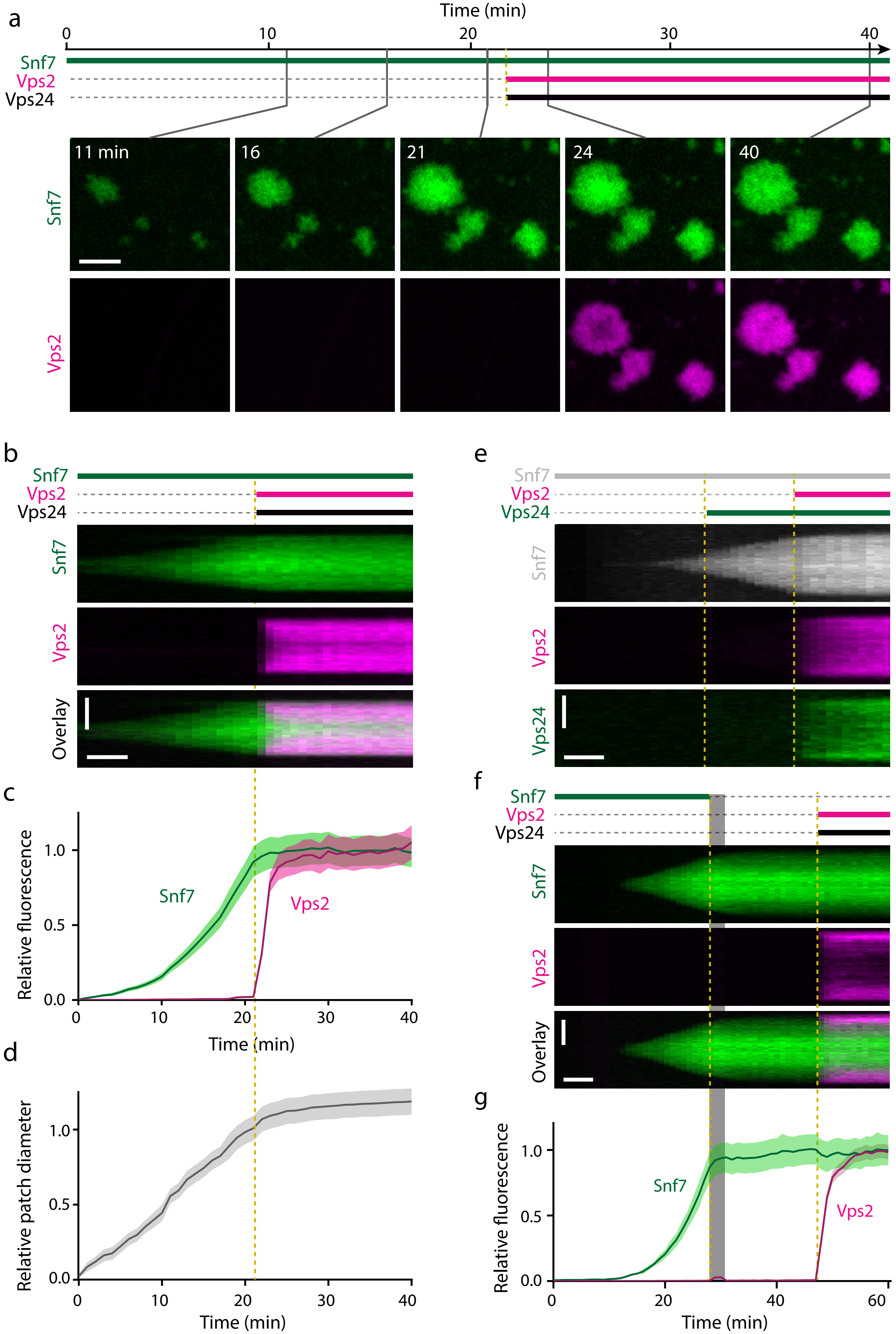

Mierzwa et al., Fig. 5

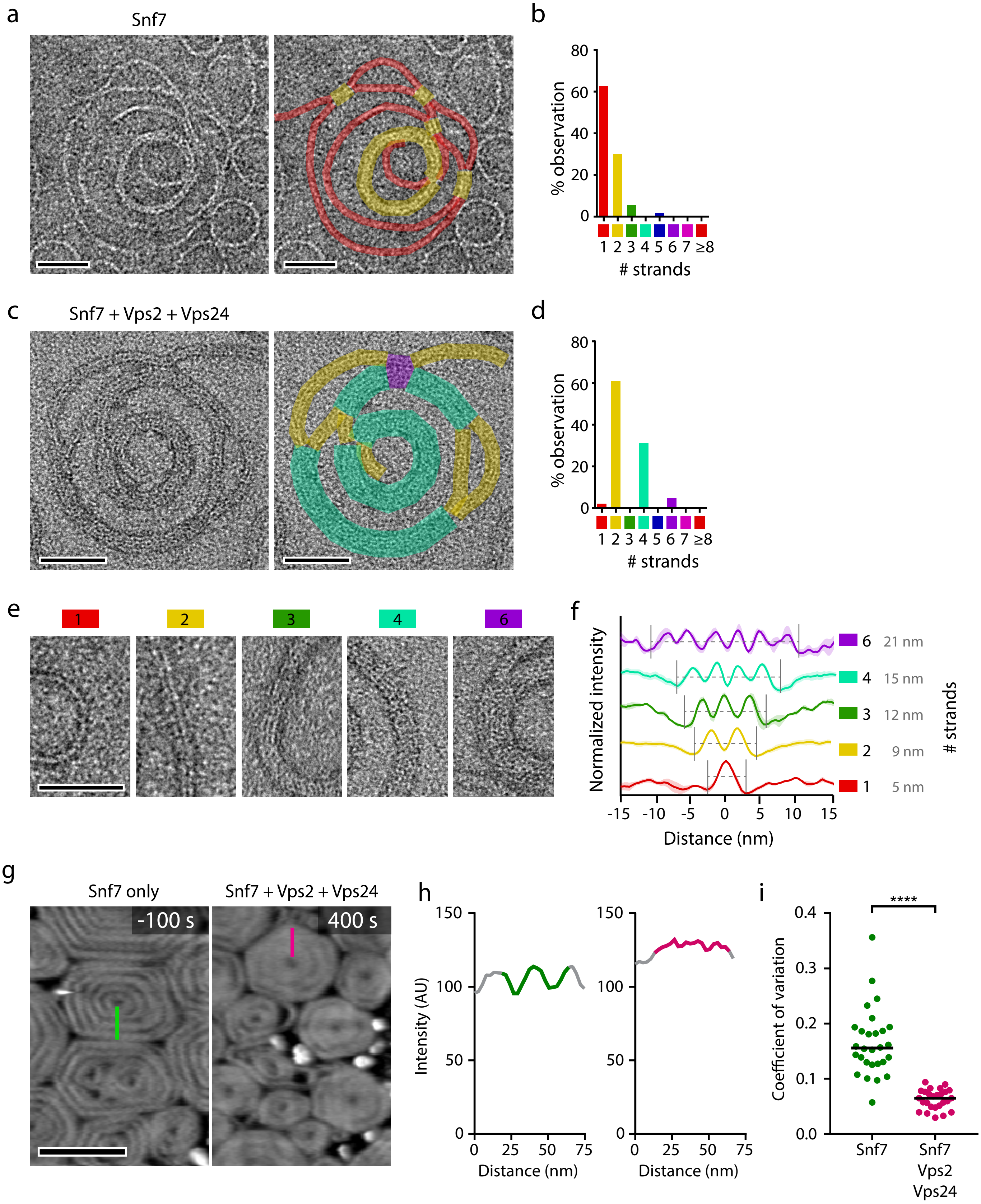

Mierzwa et al., Fig. 6

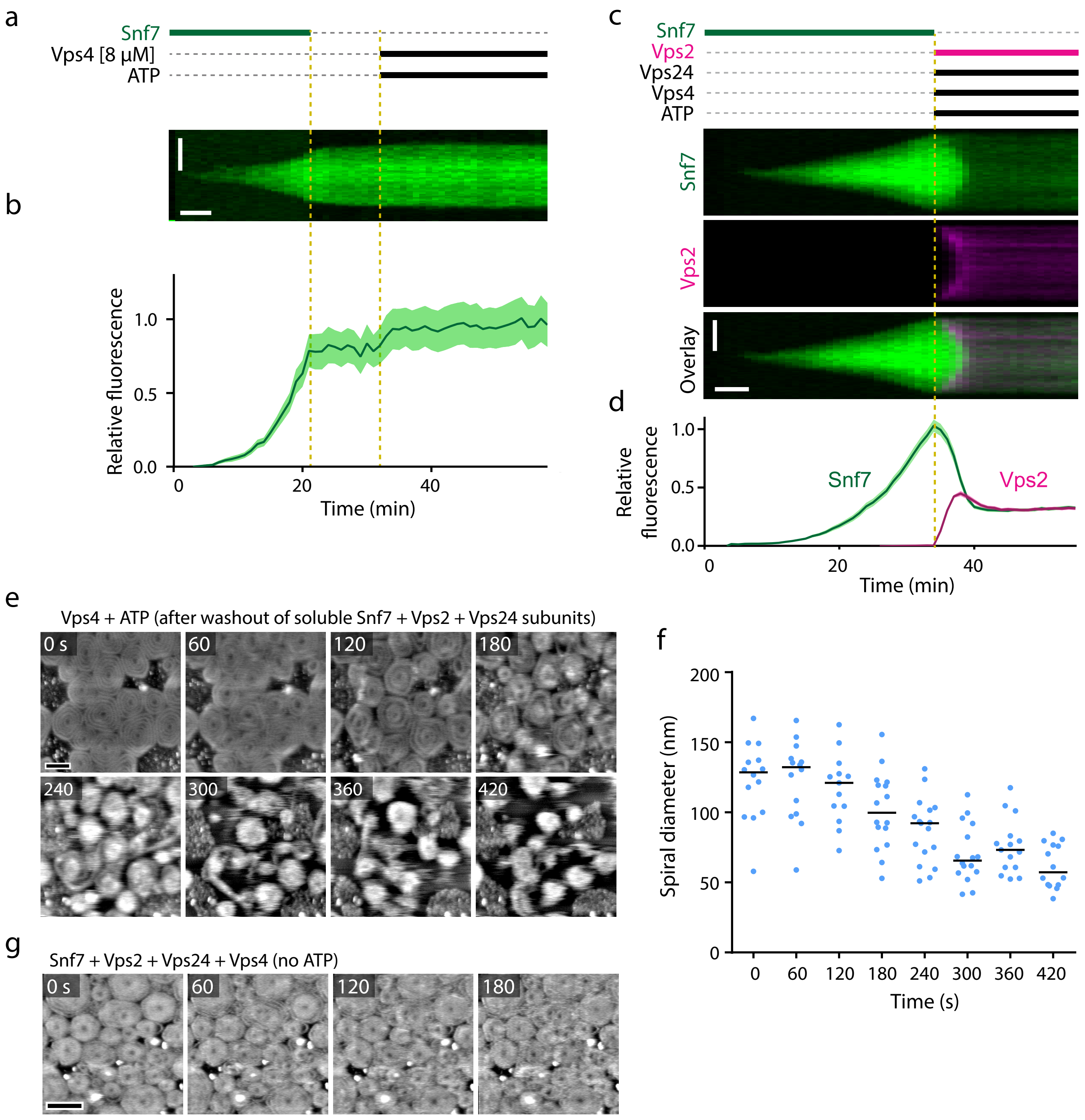

Mierzwa et al., Fig. 7

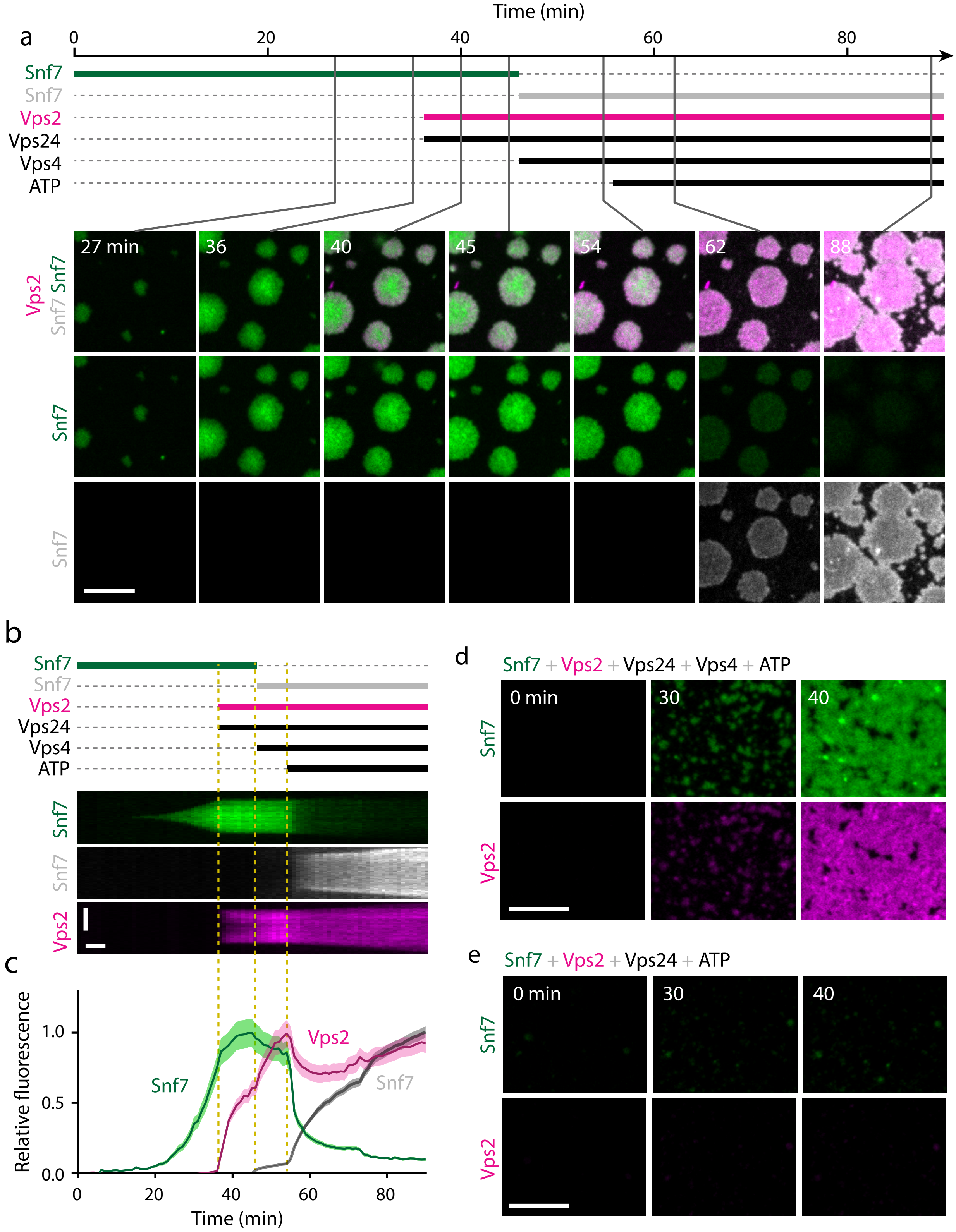
a
Time (min)
0
20
40
60
80
Snf7
Snf7
Vps2
Vps24
Vps4
ATP
27 min
36
40
45
54
62
88
Vps2 Snf7 Snf7
Snf7
Snf7
b
Snf7
Snf7
Vps2
Vps24
Vps4
ATP
Snf7
Snf7
Vps2
c
Relative fluorescence
1.0
0.5
0.0
0
20
40
60
80
Time (min)
Snf7
Vps2
Snf7
d
Snf7 + Vps2 + Vps24 + Vps4 + ATP
0 min
30
40
Snf7
Vps2
e
Snf7 + Vps2 + Vps24 + ATP
0 min
30
40
Snf7
Vps2

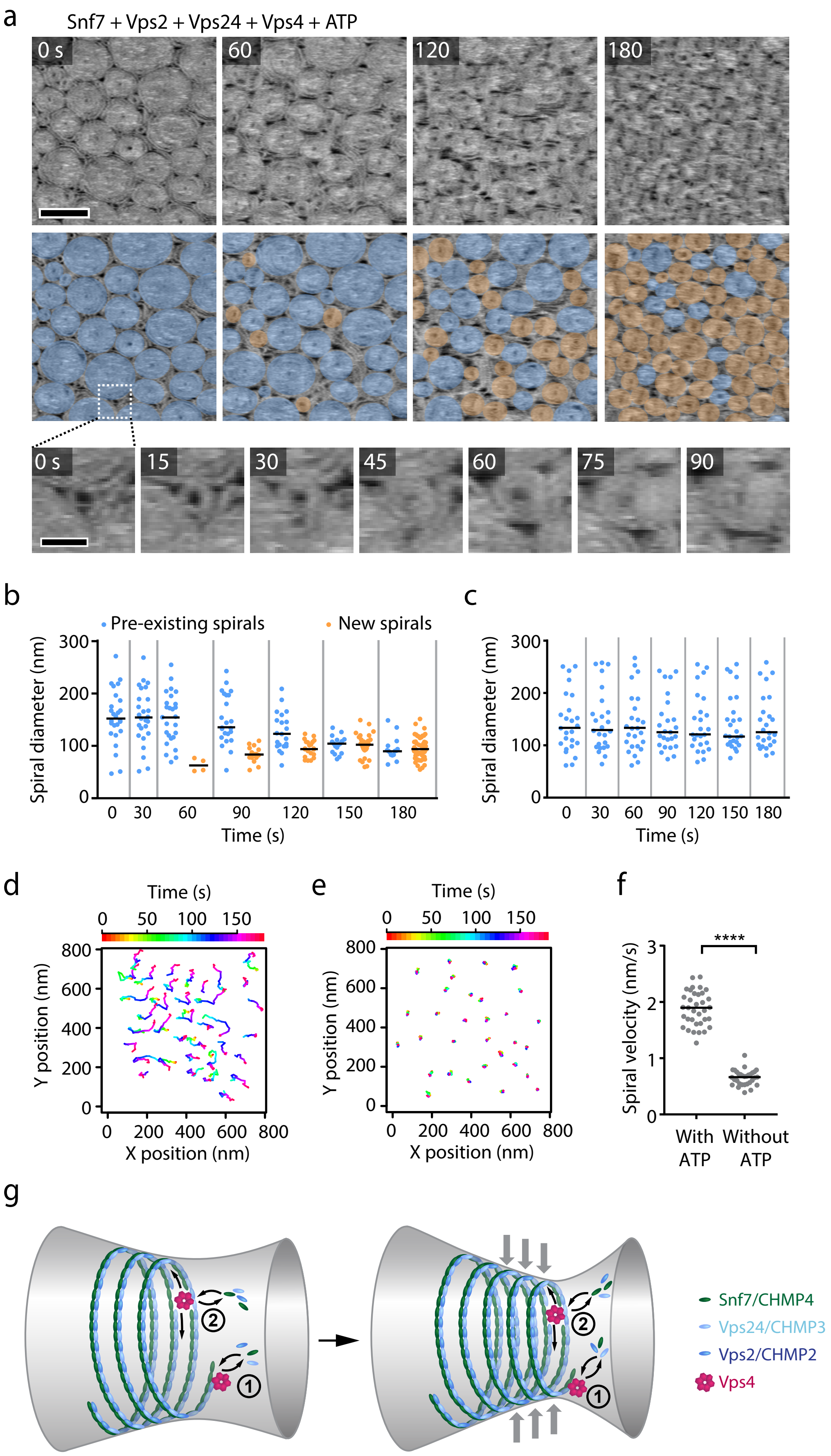Mierzwa et al., Fig. 8